Journal of Catalysis 258 (2008) 187–198

Contents lists available at ScienceDirect

Journal of Catalysis

www.elsevier.com/locate/jcat

Propene epoxidation over TiO_2-supported Au–Cu alloy catalysts prepared from thiol-capped nanoparticles

Jordi Llorca [a,*], Montserrat Domínguez [a], Cristian Ledesma [a], Ricardo J. Chimentão [b], Francisco Medina [b], Jesús Sueiras [b], Inmaculada Angurell [c], Miquel Seco [c], Oriol Rossell [c]

[a] Institut de Tècniques Energètiques, Universitat Politècnica de Catalunya, Diagonal 647, ed. ETSEIB, 08028 Barcelona, Spain
[b] Departament d'Enginyeria Química, Universitat Rovira i Virgili, 43007 Tarragona, Spain
[c] Departament de Química Inorgánica, Universitat de Barcelona, Martí i Franquès 1-11, 08028 Barcelona, Spain

ARTICLE INFO

Article history:
Received 25 April 2008
Revised 5 June 2008
Accepted 5 June 2008
Available online 11 July 2008

Keywords:
Propene epoxidation
Au–Cu alloy
Nanoparticles
HRTEM

ABSTRACT

Propene oxidation to propene oxide (PO) was performed with N_2O in the temperature range of 473–673 K using TiO_2-supported Au and Au–Cu alloy nanoparticles synthesized from pre-formed thiol-capped nanoparticles of controlled composition and size. Catalysts were activated by calcination at different temperatures in the range 573–873 K and characterized by HRTEM, XPS, and TPR. Among a series of catalysts with different Au/Cu ratio and metal loading, the Au_1Cu_3/TiO_2 with 1.2 wt% exhibited the best catalytic performance for epoxidation, both in terms of propene conversion rate and selectivity towards PO (0.25 mol PO g_M^{-1} h^{-1} at 573 K). The highest TOF was obtained over a catalyst calcined at 673 K. At this calcination temperature, HRTEM revealed a large perimeter interface between the nanoparticles and the support, which was accompanied by an intense TPR hydrogen uptake at low temperature. At increasing calcination temperature, the surface of Au–Cu alloy nanoparticles was progressively decorated with oxidized Cu species, which were detrimental for epoxidation and favored allylic oxidation products. Isolation effects and control of the extent of Cu oxidation by Au in the alloy nanoparticles as well as the perimeter interface between Au–Cu alloy nanoparticles and TiO_2 are imagined to play pivotal roles in the epoxidation of propene.

© 2008 Elsevier Inc. All rights reserved.

1. Introduction

When dispersed as fine particles of less than ~10 nm in dimension over selected metal oxides, gold exhibits exceptionally high activity in a variety of reactions such as CO oxidation, hydrogenation of CO and CO_2, water gas shift, reduction of NO to N_2, hydrogenation of unsaturated substrates, oxidation of alcohols and aldehydes, hydrochlorination of ethyne, and epoxidation of propene, among others [1–6]. Current industrial methods used for the epoxidation of propene, the chlorohydrin and organic hydroperoxide processes, have important disadvantages in terms of environmental pollution and by-products. However, propene oxide is one of the most important feedstocks for the production of many useful chemicals, such as polyurethane, polyester resins, and surfactants [7], and a process based on the direct epoxidation of propene in the gas phase using only oxygen or any other oxidant, resulting in benign side products, is highly desirable. In this context, the high catalytic activity of gold supported on TiO_2 and titanium-containing materials (such as Ti-MCM-41 and TS-1) in the direct epoxidation of propene with O_2/H_2 mixtures has attracted considerable industrial and academic interest [8–16]. The mode of operation of Au–Ti–O catalysts for this reaction remains unclear, but the role of the support, the Au particle size, and the periphery between the support and the Au particles have been recognized [11,16,17]. In particular, only the anatase form of TiO_2 leads to the formation of propene oxide, whereas the rutile form and amorphous TiO_2 cause the complete oxidation of propene into CO_2 [18]. As regards the Au particle size, there is a strong particle size dependence and only small nanoparticles (1–5 nm) are selective towards the formation of propene oxide, whereas larger Au particles increase the selectivity to combustion [9,16,19,20]. However, the high reactivity of surface-activated oxygen species generated from O_2 often leads to consecutive oxidation and, consequently, to a loss of propene oxide selectivity. For this reason, recent attention has been given to the use of nitrous oxide as a mild oxidant in the propene epoxidation reaction [21–29]. Usually N_2O is activated at metal sites, leading to N_2 and atomically adsorbed oxygen with a mild electrophilic character, suitable for the transformation of the vinyl group of propene into an oxirane ring [21,26]. In addition, N_2O is a greenhouse warming gas which is produced abundantly in industrial processes (i.e. in the production of precursors of nylon and of nitric acid) and its use in propene epoxidation, with

* Corresponding author. Fax: +34 39 401 71 49.
E-mail address: jordi.llorca@upc.edu (J. Llorca).

0021-9517/$ – see front matter © 2008 Elsevier Inc. All rights reserved.
doi:10.1016/j.jcat.2008.06.010

the only byproduct N_2, could offer an interesting solution to the environmental problems associated with this gas [28]:

$$CH_3CH{=}CH_2 + N_2O \rightarrow CH_3\underset{\diagdown\,O\,\diagup}{CH{-}CH_2} + N_2.$$

In addition to nanosized Au, it is well known that Cu-based catalysts are particularly effective for alkene epoxidation when allylic hydrogen atoms are present because Cu favors metallacycle formation instead of allylic hydrogen stripping [30,31], which is the main obstacle for epoxidation. Several examples have been reported in the literature concerning direct propene epoxidation with O_2 [32–35]. However, at sufficiently high oxygen coverage, nucleation and growth of copper oxide occurs, which inhibits epoxidation [30]. One way to control the extent of Cu oxidation under reaction conditions involves the use of alloys. It has been reported recently that Au–Cu/TiO_2 bimetallic catalysts prepared by impregnation methods perform better than Au/TiO_2 and Cu/TiO_2 for propene epoxidation [36]. However, precise control of particle size was not achieved due to the preparation route, and particles in the range 2–20 nm were encountered, which prevented accurate interpretation of the alloying effect, taking into account the dependence of propene oxide selectivity with particle size.

Several approaches have been used to prepare gold nanoparticles on metal oxide supports including incipient wetness impregnation, co-precipitation, deposition–precipitation, ion exchange, gas-phase grafting, co-sputtering, organic capping, and dendrimer and micelle encapsulation [1,2,9,37–45]. Impregnation and precipitation methods are very simple and scalable, but normally suffer from precise particle size control. In contrast, organic capping and encapsulation methods produce size-controlled gold nanoparticles whose particle size is established before deposition on the metal oxide support. Moreover, the coordinating ligands in the precursor solution and on the oxide surface prevent aggregation of the nanoparticles [12,41,46–48]. In this work, we have prepared a variety of well-defined Au and Au–Cu alloy nanoparticles with different composition and size supported on anatase from dodecanethiol-capped nanoparticles. These have been characterized by high resolution transmission electron microscopy (HRTEM), X-ray photoelectron spectroscopy (XPS), and temperature programmed reduction (TPR), and tested in the direct epoxidation of propene by N_2O. We have attempted to study the role of alloy composition as well as the contact structure between TiO_2 and the alloy nanoparticles in the propene epoxidation reaction by studying the effect of calcination temperature, particle size, and surface composition.

2. Experimental

2.1. Preparation of Au–Cu/TiO_2 catalysts

Bimetallic Au–Cu nanoparticles with Au:Cu molar ratios of 3:1, 1:1, and 1:3 as well as monometallic Au nanoparticles encapsulated with dodecanethiol monolayer shells were synthesized following the two-phase method described for the synthesis of dodecanethiol-capped monometallic Au nanoparticles [49–51] and metal alloy clusters [52]. $AuCl_4^-$ and Cu^{2+} species were first transferred from aqueous $HAuCl_4$ and $Cu(NO_3)_2$ solutions (30 mM) to toluene solution using tetraoctylammonium bromide as a phase transfer reagent. Dodecanethiol was then added to the solution at a dodecanethiol:(Au + Cu) = 3:2 mole ratio, and an excess of aqueous $NaBH_4$ was slowly added to reduce the metal salts. Bimetallic particles of different sizes were obtained by changing the concentration of metal salt solutions from 30 to 15, 6, and 3 mM. The resulting dodecanethiol-capped metallic nanoparticles were subjected to solvent removal and cleaned using ethanol. The nanoparticles were then dissolved in toluene and impregnated onto commercial anatase (Sigma–Aldrich, 99.8+%, $S_{BET} = 10\ m^2\,g^{-1}$). The solvent was evaporated slowly overnight and the samples were calcined at 573, 673, 773, or 873 K for 2 h. No organic residues were detected by thermogravimetric analysis, infrared spectroscopy, and XPS after calcination at any of these temperatures. All samples attained a pale pink color typical of the presence of gold nanoparticles over TiO_2. Au and Cu contents were measured by wet methods by inductively coupled plasma.

2.2. Characterization of catalysts

High resolution transmission electron microscopy (HRTEM) was carried out using a JEOL JEM 2010F electron microscope equipped with a field emission source at an accelerating voltage of 300 kV. Electron energy-loss spectroscopy (EELS) was performed in STEM mode with a Gatan detector. In the case of thiol-capped solutions, the sol was directly dropped onto carbon-coated grids. For Au–Cu/TiO_2 catalysts, powders were suspended in methanol for about 1 min under ultrasonic treatment before they were deposited on holey carbon-coated grids. The microscope was calibrated at different magnifications before and after measurements using appropriate standards. The point-to-point resolution achieved was 0.19 nm and the resolution between lines was 0.14 nm. A minimum of 250 particles were measured in each sample for particle size determination. The size limit for the detection of nanoparticles on the support was about 1 nm. The average particle diameter was calculated from the mean diameter frequency distribution with the formula: $d = \sum n_i d_i / \sum n_i$, where n_i is the number of particles with particle diameter d_i in a certain range. For surface analysis, X-ray photoelectron spectroscopy (XPS) was performed with a Perkin–Elmer PHI-5500 instrument equipped with an Al X-ray source operated at 12.4 kV and a hemispherical electron analyzer. Temperature programmed reduction (TPR) experiments were performed with a Thermo Finnigan TPDRO 1100 apparatus equipped with a thermal conductivity detector and coupled to a Omnistar QMS 422 mass spectrometer. A 20 mL min^{-1} gas flow of 5% H_2 in Ar was used as a reducing agent and the temperature was raised from 323 to 1073 K at a constant rate of 20 K min^{-1}.

2.3. Catalytic tests

Propene epoxidation was carried out in a fixed-bed reactor at atmospheric pressure. Experiments were carried out typically with 0.15 g of catalyst and a total flow rate between 30 and 90 mL min^{-1}. The gas mixture consisted of 10% propene and 10% N_2O balanced in Ar. The reaction was monitored at increasing temperature from 473 to 673 K. Reaction products were analyzed on-line with two gas chromatographs equipped with a molecular sieve and Porapak T columns using TCD and FID detectors. Transfer line and valves were maintained at 373 K in order to prevent condensation of products.

3. Results and discussion

3.1. Characterization of catalysts

Table 1 compiles the composition of catalysts investigated in this work. Two series of samples were prepared. In one of them, the total metal loading was maintained at ca. 1.2 wt% while the ratio Au:Cu was varied from 1:0 to 1:3 on a molar basis. In the other series, the nominal ratio Au:Cu was fixed at 1:3 and the total metal loading was varied from ca. 0.5 to 1.2 wt%. All these catalysts were characterized in detail by transmission electron microscopy techniques and XPS after calcination at different temperatures. The corresponding precursor nanoparticles were also studied by HRTEM. Details of particle size distribution of these samples are summarized in Table 2.

Table 1
Composition of catalysts calcined at 673 K and calculated alloy composition using d_{111} and d_{200} lattice spacings determined by HRTEM

Catalyst	Wt% M total	Wt% Au	Wt% Cu	Au/Cu atomic	Alloy composition
Au/TiO_2	1.21	1.21	0	–	Au_{100}
Au_3Cu_1/TiO_2	1.23	1.12	0.11	3.29	$Au_{77}Cu_{23}$
Au_1Cu_1/TiO_2	1.17	0.93	0.24	1.25	$Au_{56}Cu_{44}$
Au_1Cu_3/TiO_2	1.14	0.61	0.53	0.37	$Au_{27}Cu_{73}$
Au_1Cu_3/TiO_2 (1%)	0.98	0.49	0.49	0.32	$Au_{24}Cu_{76}$
Au_1Cu_3/TiO_2 (0.8%)	0.81	0.42	0.39	0.35	$Au_{26}Cu_{74}$
Au_1Cu_3/TiO_2 (0.5%)	0.52	0.25	0.27	0.30	$Au_{23}Cu_{77}$

3.1.1. HRTEM of nanoparticles as prepared

Fig. 1 shows a representative TEM image of nanoparticles as prepared. Homogeneous and well-dispersed particles were obtained in all cases with narrow size distributions (Fig. 1a and Table 2). It is interesting to note that, at the same metal loading, the incorporation of Cu resulted in slightly larger particles with respect to pure Au clusters (2.2–2.3 nm and 1.8 nm, respectively). Furthermore, nanoparticles obtained under increasingly diluted conditions exhibited progressively smaller size and nanoparticles of about 1.6 nm were obtained with a total metal loading of ca. 0.5% by weight. HRTEM images of individual nanoparticles as prepared are shown in Figs. 1b and 1c. Irrespectively of the Au:Cu ratio and size of nanoparticles, all of them showed lattice fringes corresponding to single face-centered cubic (fcc) phases. Lattice constant values were comprised between those of pure bulk phases of gold ($a_{Au} = 0.4079$ nm) and copper ($a_{Cu} = 0.3615$ nm), indicating that Au_xCu_{1-x} intermetallic alloys were formed.

3.1.2. Au/TiO_2 and $Au–Cu/TiO_2$ catalysts calcined at 673 K

3.1.2.1. HRTEM After deposition on TiO_2 and calcination at 673 K, nanoparticles increased in size, as expected, but a narrow size distribution in each case was maintained (Table 2). Particle growth showed a strong dependence on metal loading. The mean particle size measured in catalysts with a total metal loading of ca. 1.2% increased about 2.5–2.8 times after calcination at 673 K with respect to the size of nanoparticles as prepared, irrespective of the Au:Cu ratio. In contrast, this increase was progressively lower in those samples with lower metal content, from 2.6 and 2.5 in Au_1Cu_3/TiO_2 (1.2 and 1%) to 1.9 in Au_1Cu_3/TiO_2 (0.8%) and 1.3 in Au_1Cu_3/TiO_2 (0.5%). This resulted in TiO_2-supported Au–Cu alloy nanoparticles with the same composition, but with different particle size. Fig. 2 shows low-magnification HRTEM images of the different Au_1Cu_3/TiO_2 catalysts prepared with different metal loadings after calcination at 673 K. A range in particle size from 5.7 nm (Au_1Cu_3/TiO_2, 1.2%) to 2.1 nm (Au_1Cu_3/TiO_2, 0.5%) was obtained. In contrast, virtually the same particle size distribution (5.6–5.8 nm) was encountered in the bimetallic catalysts with the same total metal loading (1.2%) and different Au:Cu ratios after calcination at 673 K (Table 2), thus providing a suite of valuable samples for comparison of propene epoxidation.

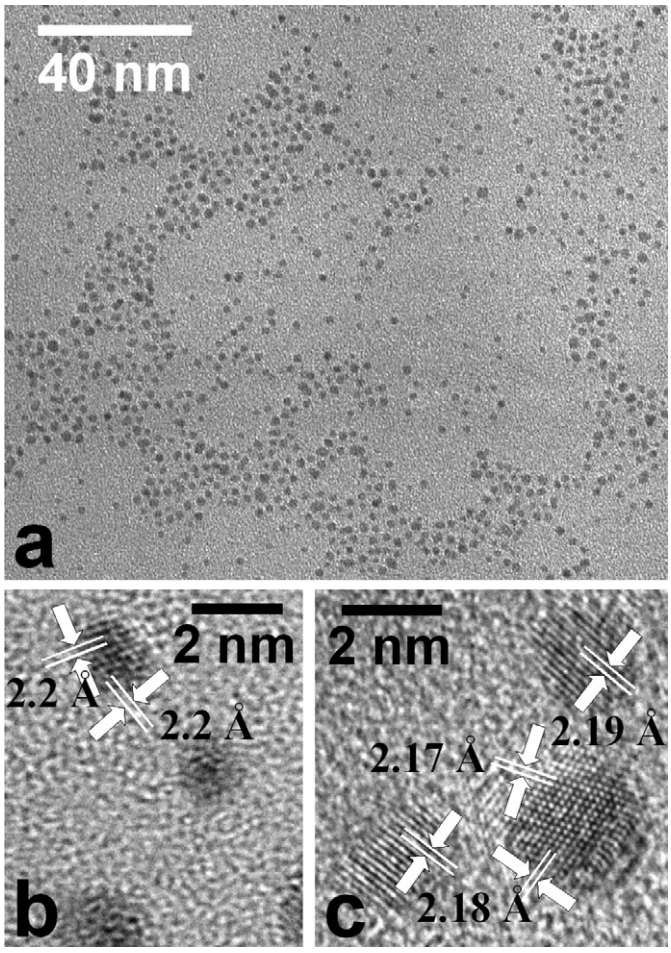

Fig. 1. (a) Bright-field TEM image of dodecanethiol-capped nanoparticles as prepared. (b, c) HRTEM images of Au_1Cu_3 alloy precursor nanoparticles of catalysts Au_1Cu_3/TiO_2 (0.5%) and Au_1Cu_3/TiO_2 (1.2%), respectively. Lattice fringes at about 2.2 Å correspond to fcc Au–Cu alloy (111) crystallographic planes.

Detailed EELS and HRTEM investigations were carried out in order to fully characterize the Au–Cu alloy nanoparticles present in each catalyst. In all cases, EEL spectra recorded over individual nanoparticles in bimetallic catalysts showed the presence of a strong signal located at 24 eV, which corresponds to the Au–Cu alloy [36]. As an example, Fig. 3 shows Z-contrast STEM images in bright and dark field modes (Figs. 3a and 3b) corresponding to catalyst Au_1Cu_1/TiO_2 and EEL spectra obtained at different locations (Figs. 3c–3f). The EEL spectrum depicted in Fig. 3c was recorded over the TiO_2 support, as corroborated by energy electron-loss signals at about 5, 12, 25, 39, and 47 eV, whereas EEL spectra in Figs. 3d–3f were recorded over individual nanoparticles labeled according to Fig. 3b. In order to gain further insight into the nature of the Au–Cu alloys present in the different catalysts, HRTEM

Table 2
Metal particle size distribution determined by HRTEM of nanoparticles as prepared and after deposition on TiO_2. Values in parenthesis indicate the range of particle size corresponding to 95% of all particles. All values in nm

Catalyst	Precursor nanoparticles	Calcination temperature (K)			
		573	673	773	873
Au/TiO_2	1.8 (1.5–2.1)	–	5.1 (4.1–6.3)	–	–
Au_3Cu_1/TiO_2	2.2 (1.7–2.5)	–	5.6 (4.4–6.5)	–	–
Au_1Cu_1/TiO_2	2.3 (2.1–2.6)	–	5.8 (4.5–6.6)	–	–
Au_1Cu_3/TiO_2	2.2 (1.6–2.4)	5.3 (4.1–6.2)	5.7 (4.4–6.8)	7.6 (5.2–11.3)	9.8 (6.7–14.5)
Au_1Cu_3/TiO_2 (1%)	2.0 (1.7–2.2)	4.2 (3.3–5.8)	4.9 (3.6–6.0)	6.8 (4.7–10.9)	9.2 (6.3–15.0)
Au_1Cu_3/TiO_2 (0.8%)	1.7 (1.4–1.9)	3.0 (2.4–3.5)	3.3 (2.0–3.6)	4.5 (3.4–8.8)	7.0 (5.5–12.4)
Au_1Cu_3/TiO_2 (0.5%)	1.6 (1.4–1.8)	2.0 (1.7–2.4)	2.1 (1.6–2.8)	3.1 (2.6–8.0)	5.8 (5.1–9.8)

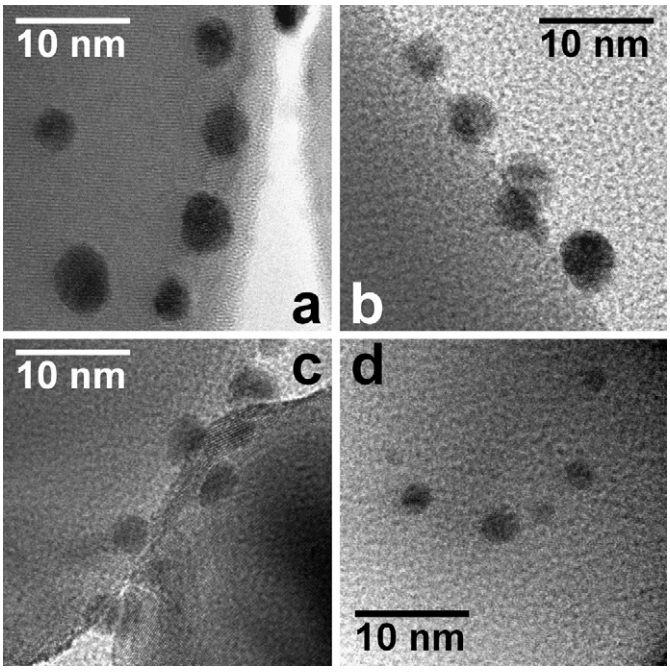

Fig. 2. HRTEM images of Au_1Cu_3 nanoparticles supported on TiO_2 and calcined at 673 K. (a) Au_1Cu_3/TiO_2 (1.2%), (b) Au_1Cu_3/TiO_2 (1.0%), (c) Au_1Cu_3/TiO_2 (0.8%), and (d) Au_1Cu_3/TiO_2 (0.5%).

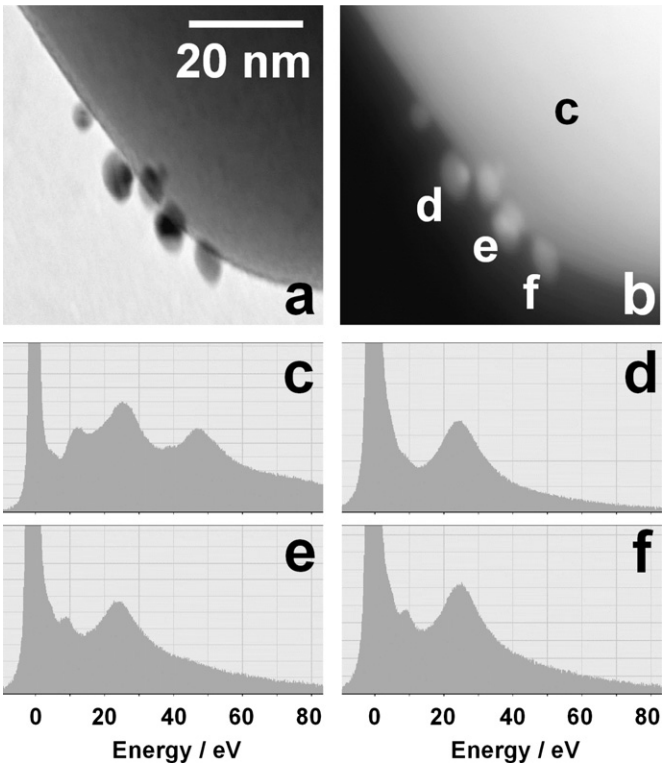

Fig. 3. Bright-field (a) and dark-field (b) STEM images of catalyst Au_1Cu_1/TiO_2 calcined at 673 K and EEL spectra recorded over areas labeled (c)–(f).

images were obtained for nearly 30 individual nanoparticles for each sample and analyzed by Fourier transform (FT) methods. As an example, Fig. 4 shows HRTEM and FT images obtained from different catalysts. Fig. 4a corresponds to catalyst Au_1Cu_3/TiO_2. Lattice fringes of the anatase support are visible at 3.52 Å, and two Au–Cu alloy particles exhibit spacings at 2.17–2.18 and 1.88 Å corresponding to fcc (111) and (200) crystallographic planes, respectively. In Fig. 4b, spots at 2.30–2.31 and 1.99 Å correspond to fcc (111) and (200) planes of an Au–Cu alloy nanoparticle of catalyst Au_3Cu_1/TiO_2. HRTEM images indicated that most particles in all samples were monocrystalline and round-shaped (Fig. 4b), whereas well-faceted particles were rarely encountered (Fig. 4a). We noted that prolonged exposure of particles under the electron beam caused structural changes, in particular, round-shaped particles became well-faceted. In order to minimize the contribution of such beam-driven effects, HRTEM images were acquired as fast as possible. Similarly to what was observed for the Au–Cu nanoparticles as prepared, TiO_2-supported alloy nanoparticles showed fcc lattice constant values intermediate to those of pure Au and Cu, indicating that the alloy structure was maintained after deposition and calcination. It is noteworthy that by this preparation route no tetragonally ordered Au–Cu phases occur, as commonly observed in Au–Cu alloys prepared by sequential implantation [53] or TiO_2-supported Au–Cu alloys prepared by conventional impregnation methods [36].

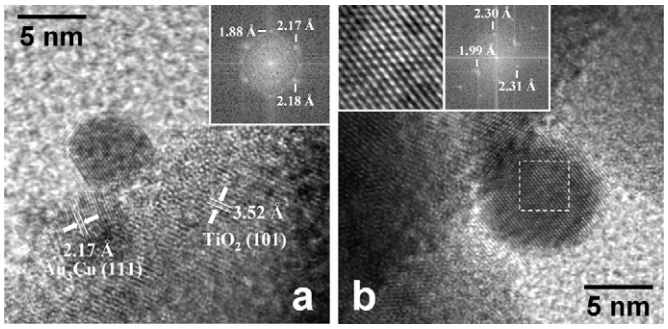

Fig. 4. HRTEM and FT images of catalysts Au_3Cu_1/TiO_2 (a) and Au_1Cu_3/TiO_2 (b) calcined at 673 K. Au–Cu alloy nanoparticles are oriented along the [110] crystallographic direction. Lattice fringes correspond to (111) and (200) planes at 2.17–2.31 and 1.88–1.99 Å, respectively.

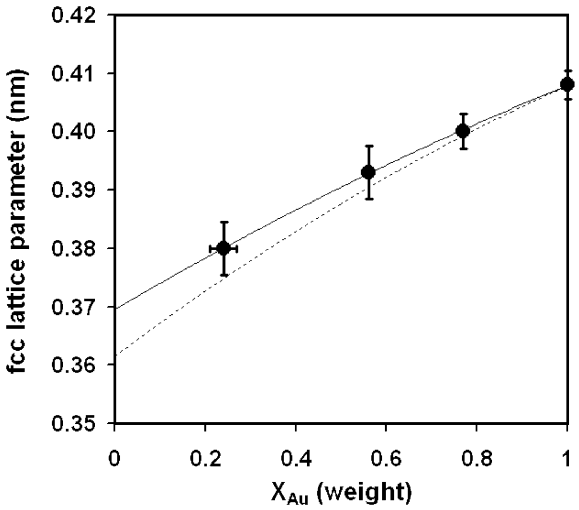

Fig. 5. Lattice parameters of fcc Au–Cu alloy nanoparticles of different composition supported on TiO_2 calculated from HRTEM (111) and (200) lattice fringe values. The dashed line corresponds to Vegard's law.

For each catalyst, a set of d_{111} and d_{200} values were compiled from all HRTEM images and the lattice constant for a cubic fcc structure was calculated. The values obtained and the corresponding error bars are plotted in Fig. 5 with respect to catalyst composition. Vegard's law ($a_{alloy} = xa_{Au} + (1-x)a_{Cu} + 0.01198x(1-x)$) [54] has also been included in the plot for comparison (dashed line). Lattice constant values decreased as the Cu content increased, according to the formation of solid solutions. The calculated alloy compositions from HRTEM measurements are included

Table 3
Binding energies and surface atomic ratios determined by XPS over catalysts calcined at 673 K

Catalyst	BE Au $4f_{7/2}$ (eV)	BE Cu $2p_{3/2}$ (eV)	Au/Ti	Cu/Ti	Au/Cu
Au/TiO_2	83.7	–	0.049	0.000	–
Au_3Cu_1/TiO_2	83.6	932.3	0.033	0.012	2.793
Au_1Cu_1/TiO_2	83.7	932.5	0.023	0.030	0.763
Au_1Cu_3/TiO_2	83.5	932.5	0.009	0.050	0.183
Au_1Cu_3/TiO_2 (1%)	83.5	932.7	0.009	0.070	0.131
Au_1Cu_3/TiO_2 (0.8%)	83.3	932.8	0.007	0.075	0.097
Au_1Cu_3/TiO_2 (0.5%)	83.2	932.7	0.004	0.058	0.065

in Table 1. Two additional trends merit highlighting. First, the higher the copper content of the catalysts, the larger the error in the measurement of the lattice constant. Second, the higher the copper content of the catalyst, the larger the deviation from Vegard's law. These trends indicate that the structure of nanoparticles is increasingly deficient in Cu as the total Cu content of the catalysts increases. This could imply that part of the copper atoms do not alloy, but remain as small clusters that escape HRTEM detection over TiO_2 or are segregated on the surface of the alloy particles. Deviations from Vegard's law have also been reported in other Au–Cu systems [36,53,54].

3.1.2.2. XPS X-ray photoelectron spectroscopy was used to investigate the oxidation states of Au and Cu and the elemental surface composition of alloy nanoparticles following synthesis and after deposition on anatase and calcination. No significant differences in elemental Au/Cu ratios and oxidation states were detected before or after deposition of nanoparticles on TiO_2 and calcination at the lowest temperature, except for the presence of sulfur, which was observed by XPS only before calcination. Table 3 compiles binding energy values and surface elemental ratios obtained over catalysts prepared with different bulk Au:Cu ratios and metal loading after calcination at 673 K. For the monometallic Au/TiO_2 sample, two sharp peaks at 87.2 and 83.7 eV were recorded, which are characteristic of spin–orbit splitting (Au $4f_{5/2}$ and $4f_{7/2}$, respectively) of Au core level spectra consistent with the Au^0 oxidation state [12,49,55]. The Au $4f_{7/2}$ binding energies recorded for the bimetallic catalysts with different bulk Au:Cu ratios, but with the same total metal loading (ca. 1.2 wt%) were virtually identical (83.5–83.7 eV), indicating that Au was in the reduced oxidation state, too. However, a slight decrease in the Au $4f_{7/2}$ binding energy was obtained over catalysts Au_1Cu_3/TiO_2 with decreasing metal loading, and values as low as 83.2 eV were obtained (Table 3). Taking into account the fact that Au is more electronegative than Cu, this could be explained by the existence of electron density transfer from copper to gold, which would result in the shifting of Au core levels towards lower binding energies [36]. This is supported by a simultaneously slight increase in Cu 2p binding energy values, from 932.5 to 932.8 eV for the Cu $2p_{3/2}$ signal (Table 3). As regards surface atomic ratios, there is a good correlation between Au/Ti and Cu/Ti values and the respective Au and Cu contents of catalysts. However, there is a substantial enrichment of copper at the surface of catalysts with respect to bulk values. This is evident from the Au/Cu elemental surface ratios reported in Table 3. A similar segregation of copper at the surface has been reported for air-exposed silica supported gold-copper clusters of about 6–7 nm [56]. In Fig. 6 the Au/Cu XPS ratios are plotted against the Au/Cu bulk ratios for the different catalysts (Table 1). Surface enrichment in copper increases as the gold content of the sample decreases (solid line). This is in accordance to HRTEM studies and lattice constant calculations reported above, where the deviation from Vegard's law increased as the Au content of catalysts decreased. On the other hand, for a given composition (Au_1Cu_3/TiO_2), there is a strong Cu segregation on the surface as the metal loading of the sample decreases. Therefore, surface enrichment in copper progressively increases as the particle size decreases.

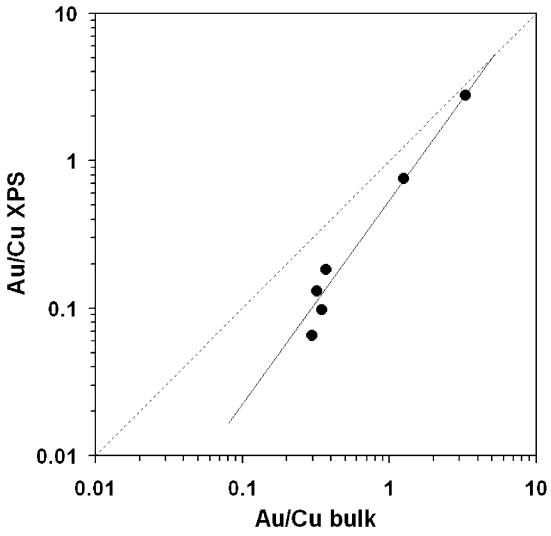

Fig. 6. Comparison of bulk and XPS atomic Au/Cu ratios recorded over catalysts with different composition calcined at 673 K. The dashed line indicates the same Au/Cu ratio for both axes.

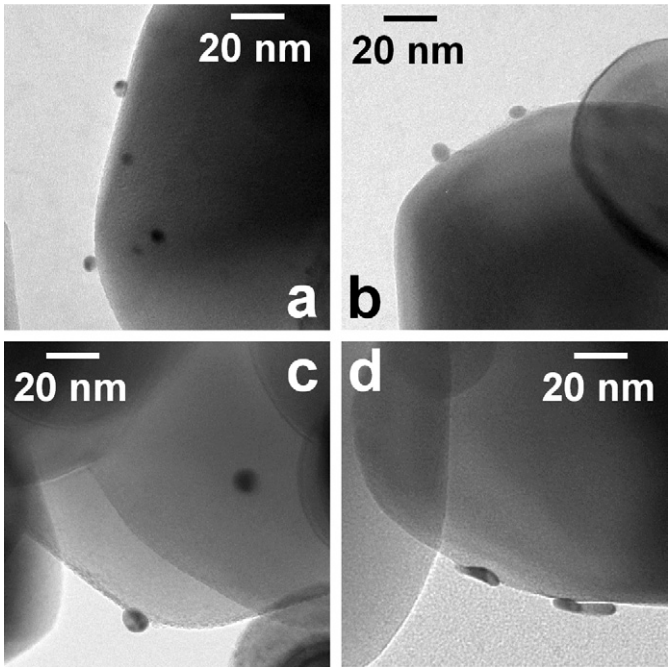

Fig. 7. Bright-field conventional TEM images of catalyst Au_1Cu_3/TiO_2 calcined at 573 (a), 673 (b), 773 (c), and 873 K (d).

3.1.3. Catalysts calcined at different temperatures

3.1.3.1. HRTEM Fig. 7 shows low-magnification, bright-field conventional TEM images obtained at the same magnification of catalyst Au_1Cu_3/TiO_2 (1.2%) calcined at different temperatures. It is evident that the calcination temperature had a strong effect on the nanoparticle size, which increased from 5.3 nm in the sample calcined at 573 K up to 9.8 nm in the sample calcined at 873 K. A more pronounced effect was observed for catalysts Au_1Cu_3/TiO_2 with lower metal loading, where the relative increase of particle size was progressively larger as the metal loading decreased (Table 2), probably due to the corresponding smaller starting particle size. Another important effect of calcination temperature con-

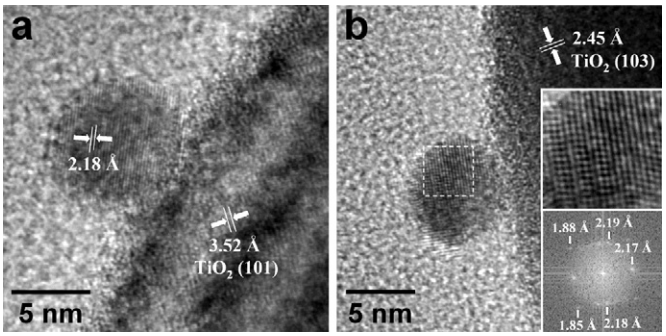

Fig. 8. HRTEM and FT images of catalyst Au_1Cu_3/TiO_2 calcined at 573 K.

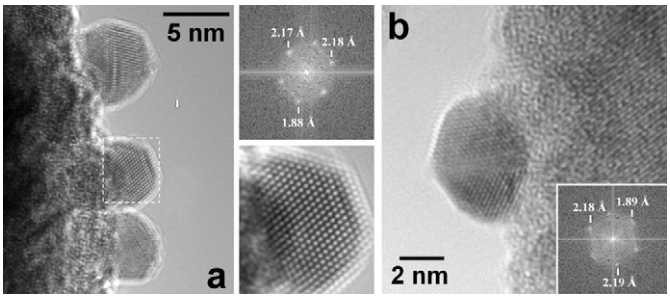

Fig. 9. HRTEM and FT images of catalyst Au_1Cu_3/TiO_2 calcined at 673 K.

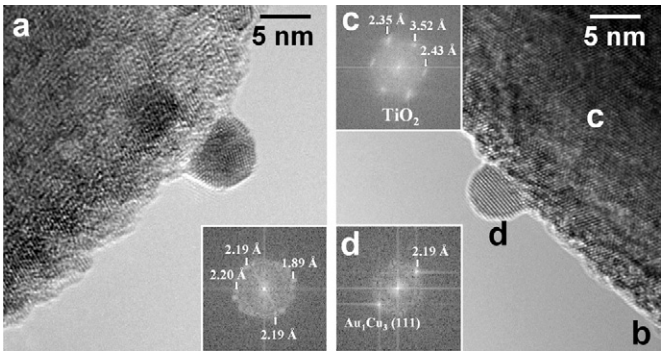

Fig. 10. HRTEM and FT images of catalyst Au_1Cu_3/TiO_2 calcined at 773 K.

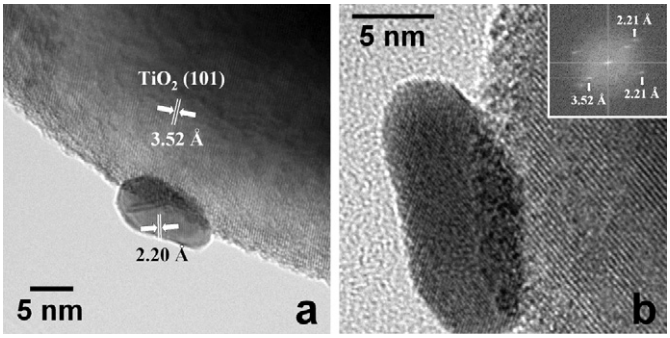

Fig. 11. HRTEM and FT images of catalyst Au_1Cu_3/TiO_2 calcined at 873 K.

cerned the morphology of the alloy nanoparticles and the contact structure between nanoparticles and the TiO_2 support. Alloy nanoparticles in catalysts calcined at 573–773 K exhibited spherical or hemispherical morphologies (Figs. 7a–7c), whereas alloy particles in the sample calcined at 873 K showed strong flattening and aggregation (Fig. 7d). Finally, the surfaces of TiO_2 crystals showed additional roughness in catalysts calcined at 673 and 773 K (Figs. 7b and 7c). From Fig. 7b it is evident that the roughness originated from the contact between the alloy nanoparticles and the anatase support, which is an indication of the existence of a strong metal–support interaction.

The interaction between alloy nanoparticles and the support as well as the alloy structure was investigated for each of these catalysts by HRTEM. Fig. 8 corresponds to the catalyst calcined at the lowest temperature, 573 K. Round-shaped particles of about 5.3 nm are well dispersed over the TiO_2 support. Lattice fringes at 2.18–2.19 and 1.85–1.88 Å correspond to fcc (111) and (200) planes of Au–Cu, respectively, in accordance with values reported for the alloy nanoparticles as synthesized. At this calcination temperature, the physical interaction between alloy nanoparticles and TiO_2 is minimum, and the contact area has a diameter of about 1.6 nm. The contact angle between nanoparticles and the support is usually $<45°$. Fig. 9 shows profile views of different alloy nanoparticles corresponding to the catalyst calcined at 673 K. Particles have increased their size slightly, from 5.3 to 5.7 nm, but now a firm contact between the alloy nanoparticles and the anatase support exists. The diameter of the contact area has notably increased to ca. 2.6 nm and the contact angle is about 60–90°. It is interesting to note in Fig. 9b that the contact region between the support and the alloy does not exhibit lattice fringes, whereas these are clearly seen both in the alloy nanoparticle as well as in the support, suggesting that the interface between them is poorly ordered at the atomic level due to a strong alloy–support interaction. The alloy nanoparticles are perfectly crystalline, as depicted in the enlarged area of Fig. 9a. From the spots in the FT images it is deduced that the lattice parameter of the Au–Cu alloy remains unchanged after calcination at 673 K. Fig. 10 corresponds to the catalyst calcined at 773 K. At this temperature the perimeter of the contact area has increased considerably with respect to samples calcined at lower temperatures and the diameter of the contact area is about 5 nm, while the mean particle size is centered at 7.6 nm. As a consequence of the stronger alloy–support interaction, the contact angle between the alloy nanoparticles and TiO_2 is greater than 90°. Lattice fringes of the alloy nanoparticles have increased slightly, 2.19–2.20 for fcc (111) planes, which may be indicative of an Au enrichment of the bulk of the alloys and Cu segregation onto the surface after calcination at 773 K. This trend is confirmed by the HRTEM images recorded over the catalyst calcined at the highest temperature, 873 K, where (111) lattice fringes up to 2.21 Å are encountered (Fig. 11). At this calcination temperature, however, the most outstanding effects are the increase in particle size and the flattened pattern exhibited by the alloy particles. Particles with axes larger than 10 nm are common, with contact areas of about 8 nm in diameter. All particles imaged by HRTEM were single-domain particles, indicating that the strong coalescence of alloy nanoparticles observed after calcination at 873 K resulted in the global rearrangement of the atoms in the structure. The FT image depicted in Fig. 11b even suggests the possibility of an epitaxial relationship between (111) planes at 2.21 Å of the Au–Cu alloy and (101) planes at 3.52 Å of TiO_2 support.

3.1.3.2. XPS X-ray photoelectron spectroscopy was carried out over catalyst Au_1Cu_3/TiO_2 (metal loading 1.2 wt%) calcined at different temperatures. The corresponding binding energies and elemental surface ratios are reported in Table 4. No differences in oxidation states were encountered in samples calcined at 573, 673 and 773 K, and binding energies for Au (83.5–83.6 eV) and Cu (932.5–932.8 eV) corresponded well to those of the reduced metals. In contrast, the binding energies recorded for the sample calcined at 873 K shifted towards higher values, which is a manifestation of charging during calcination. The binding energy value of the Au $4f_{7/2}$ peak at 84.1 eV is intermediate between Au^0 and Au^+ species, but the binding energy of Cu $2p_{3/2}$ at 933.3 eV is close to oxidized copper [57], thus indicating that significant cop-

Table 4
Binding energies and surface atomic ratios determined by XPS over catalyst Au_1Cu_3/TiO_2 (1.2%) calcined at different temperature

Calcination temperature (K)	BE Au $4f_{7/2}$ (eV)	BE Cu $2p_{3/2}$ (eV)	Au/Ti	Cu/Ti	Au/Cu
573	83.5	932.7	0.013	0.066	0.191
673	83.5	932.5	0.009	0.050	0.183
773	83.6	932.8	0.008	0.046	0.174
873	84.1	933.3	0.006	0.055	0.105

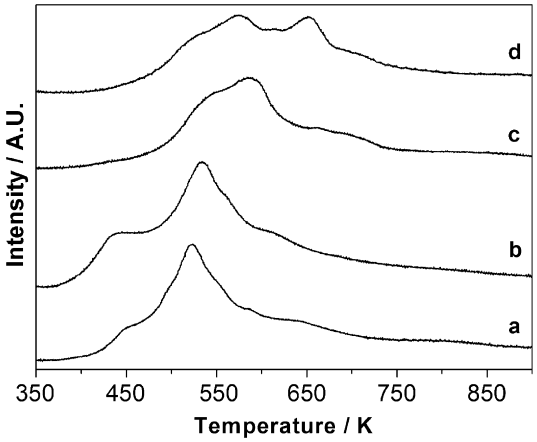

Fig. 12. TPR profiles of catalyst Au_1Cu_3/TiO_2 (1.2%) calcined at 573 (a), 673 (b), 773 (c), and 873 K (d).

per oxidation occurred at the calcination temperature of 873 K. Besides the charging effect, other phenomena took place at increasing calcination temperature, which are clearly visible in the relative Au/Cu ratios of catalysts reported in Table 4. A progressive segregation of copper on the catalyst surface was observed as the calcination temperature increased, particularly in the sample calcined at 873 K. This is in accordance with HRTEM characterization results, where the lattice parameters obtained after calcination at 773 and 873 K indicated a progressive bulk enrichment of the alloy in Au.

3.1.3.3. TPR Temperature-programmed reduction profiles obtained from catalyst Au_1Cu_3/TiO_2 (1.2% metal loading) calcined at different temperatures are shown in Fig. 12. The TPR profile recorded over the sample calcined at 573 K (Fig. 12a) showed a maximum hydrogen consumption peak at 523 K and minor consumption peaks at about 450, 585, and 645 K. The TPR profile of monometallic Cu/TiO_2 usually presents two reduction peaks centered at about 460 and 630 K [36], which are ascribed to highly dispersed CuO clusters and isolated Cu ions, respectively [34,58]. Taking into account the presence of Au in our bimetallic samples and XPS data presented above, we tentatively explain the TPR peaks at 450 and 645 K of catalyst Au_1Cu_3/TiO_2 as mainly due to highly dispersed Cu-rich ensembles. In contrast, the main hydrogen consumption peak centered at 523 K is ascribed to dissociative adsorption of hydrogen on Au–Cu alloy nanoparticles and reduction of the support surface by hydrogen spillover. Considering the metal loading, the hydrogen uptake expected if all metal was oxidized is 0.14 mmol $H_2\,g^{-1}$, whereas the real uptake was 0.21 mmol $H_2\,g^{-1}$. Taking into account that both HRTEM and XPS measurements showed the presence of metallic particles, this means that most of the hydrogen uptake in the TPR experiment correspond to hydrogen adsorbed on the alloy nanoparticles and the support. Hydrogen spillover has been demonstrated to occur over nanometer-sized gold nanoparticles supported on TiO_2 [59].

After calcination at 673 K, the TPR profile of catalyst Au_1Cu_3/TiO_2 shows two main hydrogen consumption peaks at 445 and 534 K (Fig. 12b). The general shape of the TPR profiles and the total hydrogen consumption recorded over catalyst Au_1Cu_3/TiO_2 calcined at 573 and 673 K are similar (0.21 vs 0.23 mmol $H_2\,g^{-1}$, respectively). However, the substantial increase of hydrogen consumption at low temperature merits pointing out. HRTEM and XPS data reported above showed that the increase in calcination temperature from 573 to 673 K resulted in discrete nanoparticle growth (from 5.3 to 5.7 nm), but in a strong alloy–support interaction. The remarkable intensity increase of the TPR peak at 445 K is thus likely to be explained in terms of better reducibility of the contact area between the alloy nanoparticles and TiO_2 due to a strong alloy–support interaction. The appearance of a low-temperature hydrogen consumption signal was also observed in the TPR profiles of catalysts Au_1Cu_3/TiO_2 with lower total metal loading calcined at this temperature. Fig. 13 shows the TPR profiles recorded over catalyst Au_1Cu_3/TiO_2 (1.0% metal loading) calcined at 573 and 673 K. Following calcination at 573 K, hydrogen consumption occurred at 530, 556, and 630 K (Fig. 13a), whereas calcination at 673 K resulted in a new, well-resolved hydrogen uptake signal at 500 K. Hydrogen uptake for these samples were in the range 0.16–0.20 mmol $H_2\,g^{-1}$, much higher than the theoretical value if all metal was oxidized (0.11 mmol $H_2\,g^{-1}$). Given the smaller size of nanoparticles in sample Au_1Cu_3/TiO_2 (1.0%) with respect to sample Au_1Cu_3/TiO_2 (1.2%), this large difference between the theoretical hydrogen uptake and the measured values can be explained by a large perimeter interface between the alloy nanoparticles and the support.

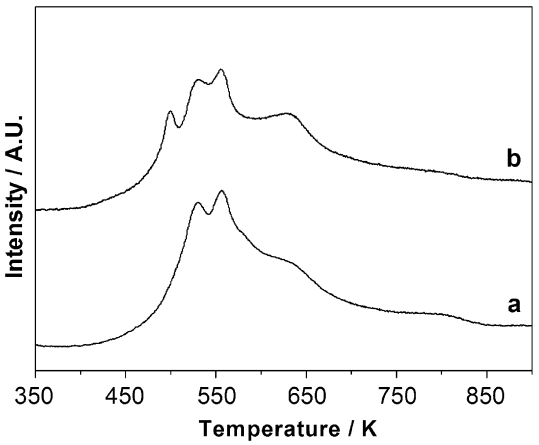

Fig. 13. TPR profiles of catalyst Au_1Cu_3/TiO_2 (1.0%) calcined at 573 (a), and 673 K (b).

TPR profiles of sample Au_1Cu_3/TiO_2 (1.2% metal loading) obtained after calcination at 773 and 873 K (Figs. 12c and 12d) exhibit similar patterns, but different to those reported at lower calcination temperature, with hydrogen consumption peaks located at about 530–535 and 575–590 K, and an additional peak at 652 K for the sample calcined at 873 K. The most remarkable difference between samples calcined at 673 and 773 K deduced from HRTEM and XPS studies is an increase of particle size, from 5.7 to 7.6 nm (Table 2), whereas similar alloy–support interaction and surface Au/Cu ratios have been reported. Therefore, the shift of the TPR signals at higher temperature could be explained in terms of size effect. In fact, it is known that the spillover of hydrogen over Au nanoparticles is progressively favored as the nanoparticle size decreases [60]. On the other hand, the increase in particle size is accompanied by a large diminution of the total number of atoms at the periphery of alloy nanoparticles, thus explaining in the disappearance of the low-temperature hydrogen consumption ascribed to the perimeter interface. Accordingly, the hydrogen uptake measured over these samples decreased to 0.16–0.17 mmol $H_2\,g^{-1}$.

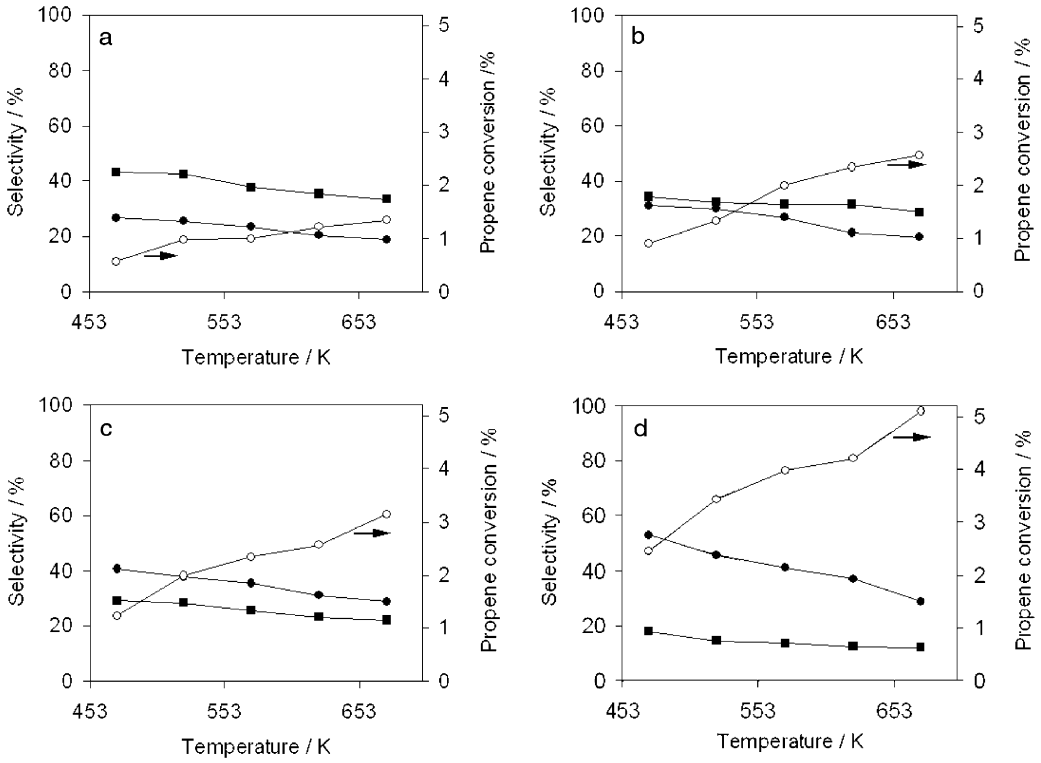

Fig. 14. Temperature dependence of the catalytic performance of Au–Cu/TiO_2 (1.2%) catalysts calcined at 673 K in propene epoxidation by N_2O. (a) Au/TiO_2, (b) Au_3Cu_1/TiO_2, (c) Au_1Cu_1/TiO_2, (d) Au_1Cu_3/TiO_2. (○) Propene conversion, (●) propene oxide selectivity, (■) acrolein selectivity. GHSV = 9000 h^{-1}.

3.2. Propene epoxidation

The direct epoxidation of propene with N_2O in the temperature range 473–673 K over the Au–Cu alloy nanoparticles supported on TiO_2 resulted in the formation of propene oxide, propanal, dimethylketone, acrolein and carbon oxides. As expected, an increase of the reaction temperature resulted in higher propene conversion, but also in lower selectivity towards the desired product, propene oxide, at the expense of total oxidation products. Total deactivation of catalysts was observed after 10 h of reaction; however, the deactivation was reversible and the activity was completely restored after a regeneration procedure at 573 K under an oxygen/helium atmosphere. We first carried out catalytic tests over Au–Cu/TiO_2 samples with different Au/Cu content and the same total metal loading (1.2%) in order to evaluate the effect of nanoparticle alloy composition on the reaction. We then continued with another set of catalytic tests over the best alloy composition with the aim of deciphering the role of catalyst calcination temperature, which, as has been demonstrated in the preceding sections, resulted in different alloy–support interaction and surface composition. Finally, we performed a similar study with samples containing lower metal loadings. No activity for the epoxidation of propene by N_2O was detected in a blank experiment carried out over TiO_2 under the same experimental conditions.

3.2.1. Effect of catalyst composition and preparation method

Fig. 14 shows the performance of catalysts containing different Au:Cu ratios and calcined at 673 K in the propene epoxidation reaction by N_2O. Among these samples, strong differences appear both in terms of propene conversion and product selectivity. Regarding propene conversion, catalysts can be ordered as follows:

$Au_1Cu_3/TiO_2 > Au_1Cu_1/TiO_2 > Au_3Cu_1/TiO_2 > Au/TiO_2$.

It should be recalled that all these catalysts contained virtually the same total metal amount (from 1.14 to 1.23 wt%, Table 1) and nanoparticles with similar size (from 5.1 to 5.8 nm, Table 2). In fact, catalyst Au_1Cu_3/TiO_2, which was about four times more active than Au/TiO_2 at 573 K, for example, had a lower metal loading and larger particles than Au/TiO_2 (1.14 vs 1.21% and 5.7 vs 5.1 nm, respectively). Therefore, it is confirmed that Au–Cu alloy particles supported on TiO_2 are much more active in the transformation of propene than Au/TiO_2. Our organic-capped nanoparticle preparation route did not allow a monometallic Cu/TiO_2 sample to be prepared, but in a previous work [36] it was demonstrated that bimetallic Au–Cu/TiO_2 systems perform better in propene epoxidation than Cu/TiO_2. Concerning catalyst selectivity, it is interesting to note that catalyst composition also had a strong influence on product distribution. In particular, the selectivity towards the desired product, propene oxide, increased strongly as the Cu content in the catalyst formulation increased (Fig. 14), and values as high as 50% at 2.5% propene conversion were reached over catalyst Au_1Cu_3/TiO_2 at 473 K. The increase in propene oxide formation was accompanied by a concomitant decrease in acrolein formation, which may result from the direct reaction between oxygen species with H atoms in the allylic position of propene or from propene oxide transformation [21,28,33]. These results suggest that site isolation effects in the Au–Cu alloy nanoparticles favor the epoxidation route or, alternatively, overcome the problem of consecutive oxidation of propene oxide. Again, samples can be ordered in terms of selectivity towards propene oxide in the following manner:

$Au_1Cu_3/TiO_2 > Au_1Cu_1/TiO_2 > Au_3Cu_1/TiO_2 > Au/TiO_2$.

Interestingly, catalytic tests conducted over catalyst Au_1Cu_3/TiO_2 under different gas hourly space velocities (GHSV) did not significantly alter product selectivity. When the residence time was varied from 0.4 to 0.8 and 1.2 s, propene conversion at 473 K increased from 2.5 to 3.1 and 5.1%, whereas propene oxide selectivity varied slightly from 53.2 to 54.3 and 51.2%, respectively.

These catalytic results can be compared with those obtained under similar experimental conditions over Au and Au–Cu catalysts obtained by conventional impregnation and reduction in H_2

Table 5
Rate of propene transformation and selectivity to propene oxide at 573 K over catalysts prepared from pre-formed nanoparticles or by conventional impregnation. In all cases samples were treated at 673 K prior to reaction

Catalyst	Rate (mmol g_M^{-1} h^{-1})		PO selectivity (%)	
	Impregnation[a]	Pre-formed[b]	Impregnation[a]	Pre-formed[b]
Au/TiO_2	9	133	7.4	23.6
Au_3Cu_1/TiO_2	22	261	12.4	26.8
Au_1Cu_1/TiO_2	45	316	23.6	35.7
Au_1Cu_3/TiO_2	49	592	26.3	41.0

[a] Data from [36].
[a] This work.

flow at 673 K [36]. The rate of propene transformation at 573 K for samples prepared by impregnation [36] and those prepared from thiol-capped nanoparticles (this work) are compiled in Table 5, as well as propene selectivity values. In all cases, Au–Cu catalysts prepared from pre-formed nanoparticles were about one order of magnitude more active on a metal basis than their respective counterparts prepared by conventional impregnation. This can be explained taking into account the fact that the samples used in this work, prepared from pre-formed Au–Cu alloys and calcined at 673 K, contained nanoparticles of about 4–7 nm in diameter (Table 2), whereas samples prepared by impregnation contained particles with broad size distributions (up to 20 nm [36]). The size effect was even more pronounced in Au/TiO_2 samples. The catalyst prepared by impregnation contained Au agglomerates in the 5–200 nm range and its activity was approximately 15 times lower than that of catalyst Au/TiO_2 prepared from thiol-capped nanoparticles, which contained well-defined Au nanoparticles of 4–6 nm in size. Due to the wide range of particle size distribution in samples prepared by impregnation, it is not possible to perform accurate turnover frequency (TOF) comparisons. In addition to catalyst activity, another point which deserves discussion is product distribution. For all catalyst formulations, selectivity towards propene oxide was considerably higher in those samples prepared from pre-formed nanoparticles with respect to samples prepared by conventional impregnation (Table 5). For example, catalyst Au_1Cu_3/TiO_2, which exhibited the best catalytic performance in propene epoxidation, yielded 41% of propene oxide at 573 K, whereas the same catalyst prepared by impregnation yielded, under the same propene conversion (4.3 vs 4.2%) and temperature, only 26.3% of propene oxide, but 32.2% of CO_x. For comparison, it has been reported very recently that a K^+-promoted 1 wt% CuO_x/SBA-15 catalyst yields 26% of propene oxide and 70% CO_x at 573 K (4.7% propene conversion) in the propene epoxidation with O_2 [35]. Therefore, catalysts prepared from pre-formed Au–Cu alloy nanoparticles are not only more active, but also more selective towards the epoxidation of propene by N_2O. In the epoxidation of propene over Au/TiO_2 in the presence of oxygen and hydrogen it has been reported that Au particles larger than 2.0 nm in diameter produce propene oxide, whereas smaller Au particles produce propane [9,19,20]. In our case, where the oxygen donor is N_2O and no hydrogen is present in the reaction mixture, Au–Cu alloy particles of about 5–6 nm in diameter produce propene oxide, whereas larger alloy particles (such as those obtained by impregnation) favor propene combustion (CO_x). Interestingly, the propene oxide formation rate over $Au–Cu/TiO_2$ alloy nanoparticles from the epoxidation of propene by N_2O is much higher than that over Au/TiO_2 using O_2/H_2 mixtures, partly because the use of N_2O as a mild oxidizing agent allows higher working temperatures (and, therefore, higher propene conversion), whereas an increase in the reaction temperature results in H_2 combustion when O_2/H_2 mixtures are employed [9,11].

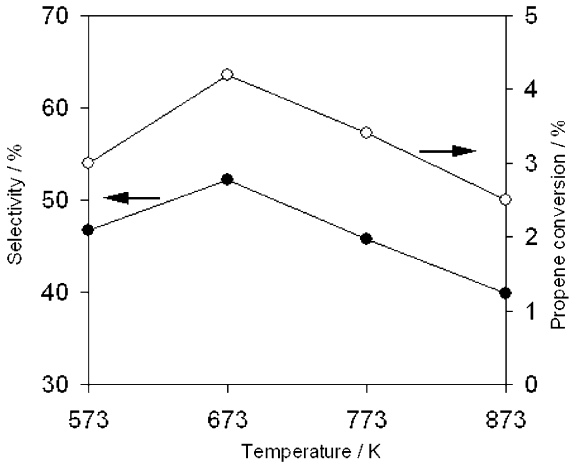

Fig. 15. Catalytic performance at 573 K of catalyst Au_1Cu_3/TiO_2 (1.2%) after calcination at 573, 673, 773, and 873 K. (○) Propene conversion, (●) propene oxide selectivity. GHSV = 9000 h^{-1}.

Table 6
Catalytic performance at 573 K of Au_1Cu_3/TiO_2 catalysts calcined at different temperature

Catalyst	T[a] (K)	χ[b] (%)	Selectivity (%)				
			PO	PA	AC	ACR	CO_x
Au_1Cu_3/TiO_2 (1.2%)	573	3.0	46.6	6.1	7.6	15.6	24.1
	673	4.2	52.2	4.4	5.8	18.0	19.6
	773	3.4	45.8	4.1	3.9	22.5	23.7
	873	2.5	39.9	3.6	4.0	22.4	30.1
Au_1Cu_3/TiO_2 (1%)	573	2.9	38.7	5.6	7.8	23.4	24.5
	673	3.3	40.1	4.7	5.9	27.2	22.1
	773	2.6	36.9	3.8	4.1	26.3	28.9
	873	1.7	30.1	2.5	3.7	28.4	35.3
Au_1Cu_3/TiO_2 (0.8%)	573	2.2	29.2	7.4	9.8	35.4	18.2
	673	1.7	32.1	6.4	7.2	35.3	19.0
	773	0.9	24.1	3.6	4.7	41.1	26.5
	873	0.3	19.7	2.1	2.3	41.8	34.1
Au_1Cu_3/TiO_2 (0.5%)	573	1.4	23.2	9.4	11.8	39.9	15.7
	673	0.9	25.6	5.7	6.1	45.8	16.8
	773	0.4	21.2	4.6	4.2	41.1	28.9
	873	0.1	19.8	2.4	3.3	37.7	36.8

Note. PO—propene oxide, PA—propanal, AC—dimethylketone, ACR—acrolein, CO_x = $CO + CO_2$. GHSV = 9000 h^{-1}.
[a] Calcination temperature.
[b] Propene conversion.

3.2.2. Effect of calcination temperature and metal loading

Catalyst Au_1Cu_3/TiO_2 (1.2%) was calcined at various temperatures and tested in the propene epoxidation reaction since it was the most active and selective sample towards the formation of propene oxide. Propene conversion and propene oxide selectivity at 573 K of samples calcined at 573, 673, 773, and 873 K are shown in Fig. 15 and a complete distribution of products is compiled in Table 6. The performance of the catalyst clearly improved when the calcination temperature was increased from 573 to 673 K, both in terms of propene conversion and propene oxide selectivity. In addition, the amount of total combustion products decreased when the calcination temperature was 673 K with respect to the sample calcined at 573 K. In contrast, an increase of the temperature of calcination up to 773 and 873 K had a negative effect on catalytic performance. Propene conversion progressively decreased at higher calcination temperature, as well as propene oxide selectivity (Fig. 15). Furthermore, an increase of the temperature of calcination from 673 to 873 K resulted in an increase of CO_x production (Table 6). These results indicate that a strong transformation occurred in the catalyst as the calcination temperature was varied

and that the best catalytic performance was obtained over the sample calcined at 673 K, both in terms of activity and selectivity towards propene oxide.

It has been shown from HRTEM that the calcination temperature has a strong influence on the microstructure of catalysts (Figs. 7–11). On one hand, the increase of the calcination temperature caused a progressive increase of the nanoparticle size (Table 2). On the other hand, higher calcination temperatures favored a strong interaction between nanoparticles and the TiO_2 support. This has been already discussed in terms of particle shape, contact angle, and support roughness. In particular, the sample calcined at 673 K, which performed better in the epoxidation of propene, exhibited only a slight increase of particle size with respect to that calcined at 573 K (5.7 vs 5.3 nm), whereas it showed enhanced alloy–support interaction. This was also supported by TPR data (Fig. 12), where the sample calcined at 673 K showed a strong uptake of hydrogen at low temperature, which was ascribed to the presence of more reactive sites, such as those expected from the interface between nanoparticles and TiO_2. At higher calcination temperatures, alloy nanoparticles increased their size considerably, from 5.7 nm for the sample calcined at 673 K to 7.6 and 9.8 nm for samples calcined at 773 and 873 K, respectively. This large increase in particle size for samples calcined at 773–873 K resulted in a strong decrease of the number of atoms located at the interface between the alloy particles and the support, which caused the disappearance of the TPR signal at low temperature. The turnover frequency (TOF) of propene oxide formation at 573 K for each calcination temperature was calculated from HRTEM results, either assuming that all surface atoms were active for propene epoxidation (Fig. 16a), or that only the perimeter interfaces around the alloy particles contributed to activity (Fig. 16b). TOF calculations strongly depend on particle size homogeneity and in some cases can lead to confusing conclusions; in our case these calculations can be considered accurate since the preparation route using pre-formed alloy nanoparticles yielded catalysts with particles exhibiting narrow size distributions and reasonably well-defined perimeter interfaces. The highest TOF value per surface atom was encountered over the Au_1Cu_3/TiO_2 (1.2%) catalyst calcined at 673 K (0.010 s^{-1}).

A slightly different pattern of TOF values vs temperature of calcination was encountered when TOF values were calculated considering only the perimeter interfaces around the alloy nanoparticles (Fig. 16b). Obviously in this case TOF values were much higher than those calculated per surface atom, and the sample calcined at 673 K yielded a TOF value for propene oxide formation of 1.33 s^{-1}. The excellent match between the pattern of TOF values calculated on a perimeter basis vs calcination temperature and that of Fig. 15, which shows propene conversion and propene oxide selectivity values obtained directly from the experiments, warrants mention. This remarkable correspondence suggests that the active sites for propene transformation are located at the contact area (interface) of alloy nanoparticles and TiO_2. A similar conclusion has been reported in the epoxidation of propene with O_2/H_2 mixtures over several gold–titania catalysts, where the active sites were ascribed to the Au–Ti interface [4,11]. In addition, explanations for the exceptional activity of Au nanostructures for CO oxidation often include a direct role played by the perimeter of the Au–support interface [60–62]. Note that the increase of propene oxide yield between samples calcined at 573 and 673 K (approximately 1.5 times) is comparable to that in propene oxide TOF values calculated considering only the perimeter interface atoms (ca. 1.2 times), but not to the increase in TOF assuming all the surface atoms (about 2.3 times). These results suggest that the catalytic behavior may be related to the extent of perimeter interface around Au–Cu alloy nanoparticles rather than the strength of the interfacial contact between alloy nanoparticles and TiO_2, as often postulated for Au/TiO_2 catalysts.

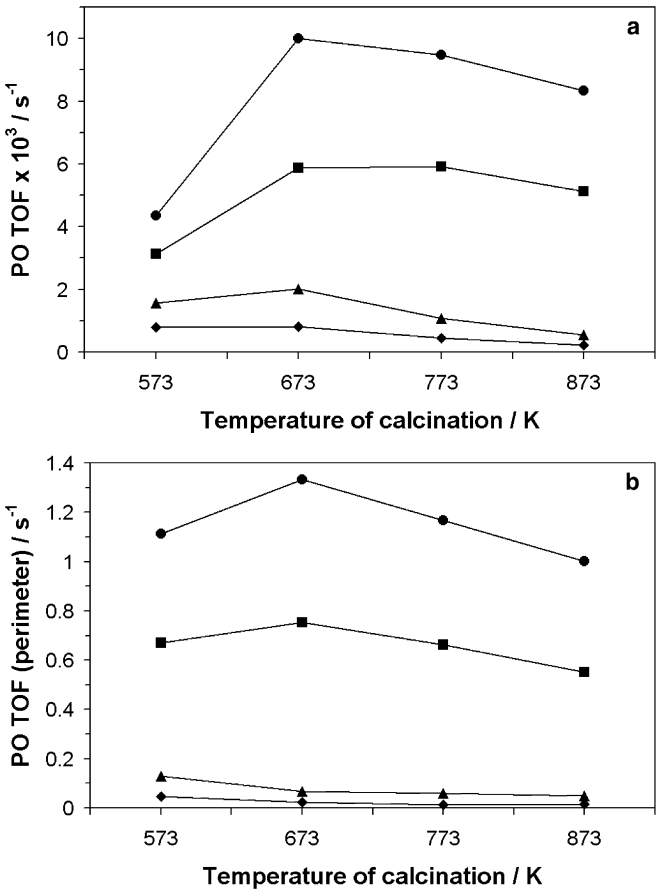

Fig. 16. Propene oxide (PO) formation rate (TOF) at 573 K over Au_1Cu_3/TiO_2 catalysts calcined at different temperatures. (a) PO TOF per surface atom, (b) PO TOF per atom at the perimeter interface. (●) Au_1Cu_3/TiO_2 (1.2%), (■) Au_1Cu_3/TiO_2 (1%), (▲) Au_1Cu_3/TiO_2 (0.8%), (◆) Au_1Cu_3/TiO_2 (0.5%). GHSV = 9000 h^{-1}.

As regards the samples calcined at 773 and 873 K, propene oxide TOF values progressively decreased at increasing calcination temperature, which cannot be explained in terms of a size increase of the alloy nanoparticles since TOF values were calculated on the basis of number of atoms exposed at the surface, or number of atoms at the perimeter. As stated in Section 3.1.3.2, XPS data indicated that the calcination temperature had a strong effect on surface composition. As the calcination temperature increased, the surface Au/Cu atomic ratio decreased and copper oxidized, that is, the catalyst surface was decorated with positively charged copper species, particularly after calcination at 873 K (Table 4). It has been reported that propene epoxidation with O_2 over Cu/SiO_2 catalysts is inhibited by Cu oxidation [30,32,33]. Therefore, our findings suggest that at a calcination temperature of 773 K or higher, the surface of Au–Cu alloy nanoparticles becomes increasingly enriched in Cu and partly oxidized, thus resulting in progressively lower TOF numbers for propene epoxidation. Fig. 17 summarizes all these changes at the microstructural level. We conclude that the calcination temperature of 673 K resulted in the best catalyst for propene epoxidation because a large alloy–support interaction took place at this temperature, while surface decoration was avoided and a small particle size was maintained, which means a large number of active sites at the perimeter of the contact area between the alloy nanoparticles and TiO_2.

The catalytic results attained at 573 K with the Au_1Cu_3/TiO_2 catalysts prepared with lower metal loadings and calcined between 573 and 873 K are included in Table 6. These are Au_1Cu_3/TiO_2

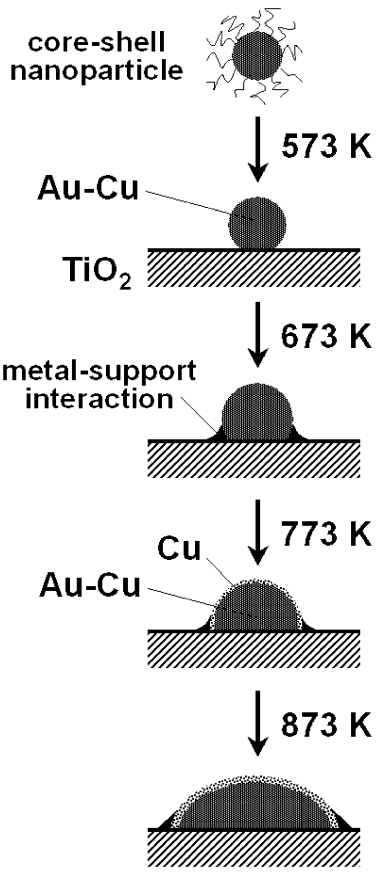

Fig. 17. Effect of calcination temperature on the structure of Au–Cu alloy nanoparticles in catalyst Au_1Cu_3/TiO_2 (1.2%). Initially, Au–Cu alloy nanoparticles are capped with an organic envelop. After deposition on TiO_2 and calcination at 573 K the organic envelop is removed but the Au–Cu alloy structure is preserved. At 673 K the size of nanoparticles increases and a strong interaction between nanoparticles and TiO_2 occurs. At 773 K there is a slight enrichment of Cu on the surface, which is more pronounced at 873 K. At this temperature the size of nanoparticles increases strongly.

(1%), Au_1Cu_3/TiO_2 (0.8%), and Au_1Cu_3/TiO_2 (0.5%). These samples had the same bulk Au/Cu ratio but differed in their particle size and surface Au/Cu values, as determined by HRTEM and XPS (Section 3.1.2). Catalyst Au_1Cu_3/TiO_2 (1%) exhibited a similar trend than that of Au_1Cu_3/TiO_2 (1.2%) discussed above, and the sample calcined at 673 K was again the most active for propene epoxidation. However, propene oxide TOF values were about 40% lower than those of Au_1Cu_3/TiO_2 (1.2%) catalyst (Fig. 16). Taking into account the fact that samples Au_1Cu_3/TiO_2 (0.8%) and Au_1Cu_3/TiO_2 (0.5%) exhibited even lower activity for propene oxide formation and that surface Au/Cu values progressively decreased as the metal loading of the samples decreased (Table 3), we conclude that decoration of the alloy nanoparticles with copper species is responsible for the low catalytic performance in propene epoxidation of these Au_1Cu_3/TiO_2 catalysts with low metal loading. It is possible that surface copper enrichment may be related to a nanoparticle size, since the alloy nanoparticles became smaller as the metal loading decreased. In fact, as the metal loading decreased and the surface was progressively enriched in Cu, the selectivity towards acrolein increased strongly at the expense of propene oxide (Table 6) and it has been reported that copper oxide is particularly active for the oxidation of propene to acrolein [32].

4. Conclusions

High yields of propene oxide can be formed through Au–Cu–Ti intimate contacting from well-defined Au–Cu alloy nanoparticles supported on anatase and calcined at 673 K. These alloy nanoparticles, with diameters of about 5–6 nm, are considerably more active and selective towards the epoxidation of propene by N_2O than their monometallic counterparts, Au/TiO_2 and Cu/TiO_2, which may be ascribed to site isolation effects caused by alloying. For samples calcined at lower temperature the interaction between alloy nanoparticles and TiO_2 is weak and low propene oxide TOF values are obtained, suggesting that the complex synergy created at the perimeter interface around Au–Cu alloy nanoparticles appears essential for epoxidation capability. However, at calcination temperatures higher than 673 K, alloy nanoparticles are progressively decorated with oxidized Cu species and the catalytic performance towards propene oxide decreases, in spite of strong particle–support interaction. This decoration effect is more pronounced with decreasing alloy particle size from ca. 5 to 2 nm, and allylic oxidation products are preferably obtained.

Acknowledgments

This work was supported by MEC grants ENE2006-06925 (J.Ll.), CTQ2006-08196 (O.R.), and CTQ2006-02362 (F.M.).

References

[1] G.C. Bond, C. Louis, D. Thompson, Catalysis by Gold, Imperial College Press, London, 2006.
[2] M. Haruta, Gold Bull. 37 (2004) 27.
[3] M. Haruta, Chem. Rec. 3 (2003) 75.
[4] M. Haruta, CATTECH 6 (2002) 102.
[5] G.C. Bond, D.T. Thompson, Appl. Catal. A Gen. 302 (2006) 1.
[6] D.T. Thompson, Top. Catal. 38 (2006) 231.
[7] T.A. Nijhuis, M. Makkee, J.A. Moulijn, B.M. Weckhuysen, Ind. Eng. Chem. Res. 45 (2006) 3447.
[8] M. Haruta, N. Yamada, T. Kobayashi, S. Iijima, J. Catal. 115 (1989) 301.
[9] T. Hayashi, K. Tanaka, M. Haruta, J. Catal. 178 (1998) 566.
[10] Y.A. Kalvachev, T. Hayashi, S. Tsubota, M. Haruta, J. Catal. 186 (1999) 228.
[11] E.E. Stangland, K.B. Stavens, R.P. Andres, W.N. Delgass, J. Catal. 191 (2000) 332.
[12] J. Chou, E.W. McFarland, Chem. Commun. (2004) 1648.
[13] E. Sacaliuc, A.M. Beale, B.M. Weckhuysen, T.A. Nijhuis, J. Catal. 248 (2007) 235.
[14] A.K. Sinha, S. Seelan, M. Okumura, T. Akita, S. Tsubota, M. Haruta, J. Phys. Chem. B 109 (2005) 3956.
[15] B. Chowdhury, J.J. Bravo-Sárez, M. Daté, S. Tsubota, M. Haruta, Angew. Chem. Int. Ed. 45 (2006) 412.
[16] J. Lu, X. Zhang, J.J. Bravo-Suárez, K.K. Bando, T. Fujitani, S.T. Oyama, J. Catal. 250 (2007) 350.
[17] C. Sivadinarayana, T.V. Chouhary, L.L. Daemen, J. Eckert, D.W. Goodman, J. Am. Chem. Soc. 126 (2004) 38.
[18] M. Haruta, B.S. Uphade, S. Tsubota, A. Miyamoto, Res. Chem. Intermed. 24 (1998) 329.
[19] M. Haruta, M. Daté, Appl. Catal. A Gen. 222 (2001) 427.
[20] A.K. Sinha, S. Seelan, S. Tsubota, M. Haruta, Angew. Chem. Int. Ed. 43 (2004) 1546.
[21] V. Duma, D. Hönicke, J. Catal. 191 (2000) 93.
[22] E. Ananieva, A. Reitzmann, Chem. Eng. Sci. 59 (2004) 5509.
[23] X. Wang, Q. Zhang, S. Yang, Y. Wang, J. Phys. Chem. B 109 (2005) 23500.
[24] Q. Zhang, Q. Guo, X. Wang, T. Shishido, Y. Wang, J. Catal. 239 (2006) 105.
[25] A. Costine, T. O'Sullivan, B.K. Hodnett, Catal. Today 112 (2006) 103.
[26] Y. Wang, W. Yang, L. Yang, X. Wang, Q. Zhang, Catal. Today 117 (2006) 156.
[27] T. Thömmes, S. Zürcher, A. Wix, A. Reitzmann, B. Kraushaar-Czarnetzki, Appl. Catal. A Gen. 318 (2007) 160.
[28] B. Moens, H.D. Winne, S. Corthals, H. Poelman, R. De Gryse, V. Meynen, P. Cool, B.F. Sels, P.A. Jacobs, J. Catal. 247 (2007) 86.
[29] S. Yang, W. Zhu, Q. Zhang, Y. Wang, J. Catal. 54 (2008) 251.
[30] R.M. Lambert, F.J. Williams, R.L. Cropley, A. Palermo, J. Mol. Catal. A Chem. 228 (2005) 27.
[31] D. Torres, N. Lopez, F. Illas, R.M. Lambert, Angew. Chem. Int. Ed. 46 (2007) 2055.
[32] J. Lu, M. Luo, H. Lei, X. Bao, C. Li, J. Catal. 211 (2002) 552.
[33] O.P.H. Vaughan, G. Kyriakou, N. Macleod, M. Yikhov, R.M. Lambert, J. Catal. 236 (2005) 401.
[34] H. Chu, L. Yang, Q. Zhang, Y. Wang, J. Catal. 241 (2006) 225.
[35] Y. Wang, H. Chu, W. Zhu, Q. Zhang, Catal. Today 131 (2008) 496.
[36] R.J. Chimentao, F. Medina, J.L.G. Fierro, J. Llorca, J.E. Sueiras, Y. Cesteros, P. Salagre, J. Mol. Catal. A Chem. 274 (2007) 159.
[37] Q. Fu, H. Saltsburg, M. Flytzani-Stephanopoulos, Science 301 (2003) 935.

[38] C. Mohr, H. Hofmeister, J. Radnik, P. Claus, J. Am. Chem. Soc. 125 (2003) 1905.
[39] B.L.V. Prasad, S.I. Stoeva, C.M. Sorensen, K.J. Klabunde, Langmuir 18 (2002) 7515.
[40] J.P. Spatz, S. Mössmer, C. Hartmann, M. Möller, T. Herzog, M. Krieger, H.-G. Boyen, P. Ziemann, B. Kabius, Langmuir 16 (2000) 407.
[41] J. Chou, N.R. Franklin, S.-H. Baeck, T.F. Jaramillo, E.W. McFarland, Catal. Lett. 95 (2004) 107.
[42] R. Zanella, S. Giorgio, C.R. Henry, C. Louis, J. Phys. Chem. B 106 (2002) 7634.
[43] L.D. Menard, F. Xu, R.G. Nuzzo, J.C. Yang, J. Catal. 243 (2006) 64.
[44] K. Mallick, M.J. Witcomb, M.S. Scurrell, Appl. Catal. A Gen. 259 (2004) 163.
[45] J.-D. Grunwaldt, M. Maciejewski, O.S. Becker, P. Fabrizioli, A. Baiker, J. Catal. 186 (1999) 458.
[46] A.C. Templeton, W.P. Wuelfing, R.W. Murray, Acc. Chem. Res. 33 (2000) 27.
[47] C.-J. Zhong, M.M. Maye, Adv. Mater. 13 (2001) 1507.
[48] M.M. Maye, J. Luo, L. Han, N.N. Kariuki, C.-J. Zhong, Gold Bull. 36 (2003) 75.
[49] M. Brust, M. Walker, D. Bethell, D.J. Schiffrin, R. Whyman, J. Chem. Soc. Chem. Commun. (1994) 801.
[50] C.J. Kiely, J. Fink, J.G. Zheng, M. Brust, D. Bethell, D. Schiffrin, J. Adv. Mater. 12 (2000) 640.
[51] J. Llorca, A. Casanovas, M. Domínguez, I. Casanova, I. Angurell, M. Seco, O. Rossell, J. Nanoparticle Res. 10 (2008) 537.
[52] M.J. Hostetler, C.-J. Zhong, B.K.H. Yen, J. Anderegg, S.M. Gross, N.D. Evans, M. Porter, R.W. Murray, J. Am. Chem. Soc. 120 (1998) 9396.
[53] G. Battaglin, E. Cattaruzza, F. Gonella, G. Mattei, P. Mazzoldi, C. Sada, X. Zhang, Nucl. Instrum. Methods Phys. Res. B 166–167 (2000) 857.
[54] G. De, C.N.R. Rao, J. Phys. Chem. B 107 (2003) 13597.
[55] H.G. Boyen, G. Kästle, Science 297 (2002) 1533.
[56] G. Meitzner, G.H. Via, F.W. Lytle, J.H. Sinfelt, J. Chem. Phys. 83 (1985) 4793.
[57] A.Q. Wang, J.H. Liu, S.D. Lin, T.S. Lin, C.Y. Mou, J. Catal. 233 (2005) 186.
[58] S. Velu, K. Susuki, M. Okasaki, M.P. Kapoor, T. Osaki, F. Ohashi, J. Catal. 194 (2000) 373.
[59] S. Schimpf, M. Lucas, C. Mohr, U. Rodemerck, A. Brückenr, J. Radnik, H. Hofmeister, P. Claus, Catal. Today 72 (2005) 63.
[60] S. Tsubota, T. Nakamura, K. Tanaka, M. Haruta, Catal. Lett. 56 (1998) 131.
[61] J.-D. Grunwaldt, C. Kiener, C. Wögerbauer, A. Baiker, J. Catal. 181 (1999) 223.
[62] M.S. Chen, D.W. Goodman, Science 306 (2004) 252.